Spatial input–output analysis of large-scale structures in actuated turbulent boundary layers

Chang Liu[1] and Igal Gluzman[2]
Johns Hopkins University, Baltimore, MD, 21218

Mitchell Lozier[3], Samaresh Midya[3], Stanislav Gordeyev[4], and Flint O. Thomas[5]
University of Notre Dame, Notre Dame, IN, 46556

Dennice F. Gayme[6]
Johns Hopkins University, Baltimore, MD, 21218

Introducing a controlled external actuation has been shown to provide important insight into the dynamics of turbulent boundary layers. Input-output (resolvent) analysis provides an important tool for the analysis of the actuated flow field, but the decomposition leads to an ambiguity in determining a streamwise wavenumber associated with the spatially localized external actuation. This paper proposes spatial input–output analysis based on the recently developed one-way spatial integration in which the problem is reformulated in terms of spatial evolution equations that do not require specification of the streamwise wavenumber of interest. This downstream marching has the added benefit of embedding a wall-normal dependent convective velocity for actuated large-scale structures associated with a dominant temporal frequency. We use this framework to examine the effect of localized periodic actuation at a given temporal frequency, which is modeled as a streamwise body force associated with that frequency. The results are compared with experiments featuring an active large-scale structures actuator. The large-scale structures associated with the modal velocity field obtained from spatial input-output analysis are shown to closely match those associated with the phase-locked velocity computed based on hot-wire measurements. We then analyze the downstream propagation of these structures. We show that the model captures the decrease in inclination angle that arises from the variation in the convective velocity over the wall-normal extent. These results highlight the promise of a spatial framework in modeling and analyzing the formation and streamwise evolution of large-scale structures induced by a spatially localized perturbation with a dominant temporal frequency.

I. Introduction

Large-scale structures in turbulent boundary layers (TBL) are known to contribute significantly to the turbulent kinetic energy and Reynolds stress production [1, 2] that influence the near-wall small-scale structures [3–5] and local skin friction [6]. Large-scale structures can also be manipulated to change the properties of the boundary layer e.g. to reduce drag in a high Reynolds number TBL [7]; see e.g., review [8]. Therefore, understanding their dynamics and interactions with the overall TBL can provide insight into both the underlying physics and flow control strategies for drag-reduction.

The dynamics of large-scale structures can be studied by analyzing the flow response to an external large-scale perturbation. This approach dates back to Hussain and Reynolds [9, 10], where a thin vibrating ribbon near the wall is used to introduce perturbations into turbulent channel flow. They analyzed the experimental results by introducing a triple decomposition of the instantaneous velocity into a temporal mean, phase-locked harmonic perturbations (organized waves), and the remaining turbulence. Periodic perturbations can be also experimentally introduced into a turbulent

---

[1]Graduate student, Department of Mechanical Engineering
[2]Postdoc fellow, Department of Mechanical Engineering
[3]Graduate student, Department of Aerospace and Mechanical Engineering, AIAA Student member
[4]Associate Professor, Department of Aerospace and Mechanical Engineering, AIAA Associate Fellow
[5]Professor, Department of Aerospace and Mechanical Engineering, AIAA Associate Fellow
[6]Associate Professor, Department of Mechanical Engineering

boundary layer through a dynamic (temporally oscillating) roughness, which provides a reference phase to isolate synthetic large-scale structures and small-scale flow structures [11–14]. Instead of introducing the perturbation very close to the wall, Ranade et al. [15] performed the experimental study where the perturbation is introduced at the outer region as a forced shear layer. Focusing on the perturbation within the region of boundary layer thickness, Lozier et al. [16, 17, 18] further introduced large-scale perturbations through a dielectric barrier discharge (DBD) plasma actuator and performed phase-locked decomposition to obtain synthetic large-scale structures and to investigate its interactions with the residual turbulence.

Modeling large-scale structures due to external periodic perturbation can also date back to Reynolds and Hussain [19], where various closure models are employed to modify the Orr-Sommerfeld equation describing the evolution of organized waves in turbulent channel flows. Jacobi and McKeon [12] further compared the phase-locked velocity measured in TBL perturbed by dynamic roughness with the prediction from the resolvent analysis [20], which was shown to provide a reasonably accurate prediction.

In the above experiments, the dominant temporal frequency of the perturbation is introduced that directly determines the frequency for the velocity decomposition, analysis, and modeling of the phenomena. However, how to choose a suitable streamwise wavenumber is not fully understood. There have been a number of methods used to determine the streamwise wavenumber of interest. For example, Jacobi and McKeon [12] determined the streamwise wavenumber based on a least-squares fit over the several downstream measurements for modeling of synthetic large-scale structures using resolvent analysis. However, the spatially localized perturbations introduced into the flow also breaks the shift-invariance in the streamwise direction that suggests characterizing the streamwise variation by a complex wavenumber to include the downstream growing or decaying [12, 21]. It was also shown that a single frequency perturbation is associated with broadband streamwise wavenumber [21]. If we employ an estimation using Taylor's frozen turbulence hypothesis [22], the single frequency that is introduced through the perturbation will result in different streamwise wavenumber at different wall-normal heights depending on their local mean velocity [12, 21].

An alternative approach to obtaining this information without the limitation to a single streamwise wavenumber is to perform analysis based on downstream marching in the streamwise direction rather than the typical temporal evolution equations. Spatial equations do not require empirical determination of a streamwise wavenumber as they inherently represent the behavior across the streamwise spectra and also suitable to describe flow response due to spatially localized actuation. However, directly converting temporal marching equations into spatial marching will lead to ill-posed problems that require regularizations to obtain a well-posed PDE [23, 24]. One-way spatial integration of hyperbolic equations, recently developed by Towne and Colonius [25], provide a well-posed one-way approximation of linear hyperbolic systems.

In this work, we propose spatial input–output analysis based on recently developed one-way spatial integration [25] for the modeling of large-scale structures in the actuated turbulent boundary layer. This downstream marching embeds a wall-normal dependent convective velocity for actuated large-scale structures associated with a dominant temporal frequency. The effect of the plasma actuator is modeled as a streamwise body force associated with a dominant temporal frequency. The magnitude of this body force is modeled as a Dirac delta function in the streamwise direction, a Gaussian function in the wall-normal direction, and uniform in the spanwise direction. The results are compared with large-scale structures in experimental measurements, where the perturbation is introduced through a dielectric barrier discharge plasma actuator. The shape of large-scale structures is obtained through measurements from hot-wire anemometry and a phase-locked analysis. Large-scale structures obtained from this spatial input–output analysis show qualitative agreements with experimental measurements. We then employ this framework to examine the flow response of the actuated large-scale structures propagating downstream. The structures are shown to be more inclined towards the wall at downstream resulting from different convective velocities dependent on the distance from the wall. The wall-normal velocity is instead nearly uniform across the channel height. We also apply the quadrant analysis [26, 27] to results of actuated large-scale structures, and its quadrant trajectory order shares similarity to observation in turbulent pipe flows [28], which implies that our actuation creates structures consistent with those in canonical wall-bounded turbulent flows. This work shows the promise of a spatial framework in modeling and analyzing large-scale structures induced by a spatially localized perturbation with a dominant temporal frequency.

The remainder of this paper is organized as follows. Section II describes the spatial input–output analysis framework. In Section III, we present experimental setup to obtain the actuated large-scale structures and compare these with results obtained from this spatial input–output analysis. Section IV further employs this spatial input-output analysis to analyze the downstream evolution of actuated large-scale structures. Section V concludes this paper.
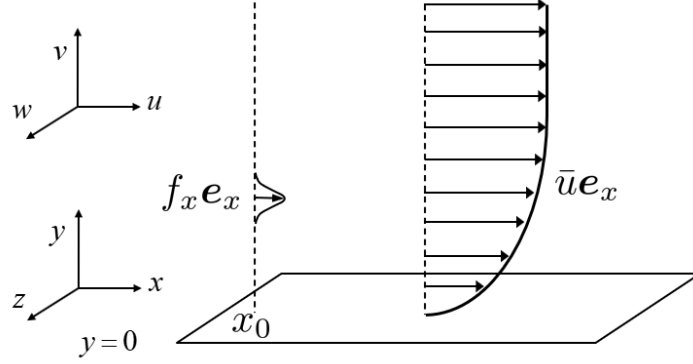
2

Fig. 1   Illustration of an actuated turbulent boundary layer.

II. Spatial input–output analysis of an actuated turbulent boundary layer

In order to model the flow response of actuated turbulent boundary layer as shown in figure 1, we consider incompressible flow above an infinite parallel plate driven by a streamwise pressure gradient, where x, y, z are the streamwise, wall-normal, and spanwise directions, respectively. Here, we invoke the quasi-parallel assumption that the streamwise variation of mean velocity is negligible, which was quantified as a reasonable assumption by spatio-temporal measurement [21]. We decompose the velocity field, $\boldsymbol{u}_{\text{tot}} = \begin{bmatrix} u_{\text{tot}} & v_{\text{tot}} & w_{\text{tot}} \end{bmatrix}^{\text{T}}$ and the pressure field, p_{tot} into mean and fluctuating quantities $\boldsymbol{u}_{\text{tot}} = \bar{u}(y)\boldsymbol{e}_x + \boldsymbol{u}$ and $p_{\text{tot}} = \bar{p} + p$, where $^{\text{T}}$ indicating the transpose, $\boldsymbol{e}_x$ denoting the streamwise unit vector and, the overbars representing time-averaged quantities, $\bar{\phi} = \lim_{T \to \infty} \frac{1}{T} \int_0^T \phi(t)\, dt$.

Then, we employ streamwise body force $f_x \boldsymbol{e}_x$ to model the effect of the plasma actuation, while we neglect the body force induced by the plasma actuator in the wall-normal or spanwise directions. The dynamics of the fluctuations $\boldsymbol{u}$ and p linearized around the turbulent mean velocity forced by this streamwise forcing $f_x \boldsymbol{e}_x$ is governed by:

$$\partial_t \boldsymbol{u} + \bar{u}\partial_x \boldsymbol{u} + v\frac{d\bar{u}}{dy}\boldsymbol{e}_x + \frac{\boldsymbol{\nabla} p}{\rho} - \nu\nabla^2 \boldsymbol{u} = f_x \boldsymbol{e}_x, \tag{1a}$$

$$\boldsymbol{\nabla} \cdot \boldsymbol{u} = 0. \tag{1b}$$

In equation (1), ρ is the density of the fluid, ν is kinematic viscosity. The friction velocity is defined as $u_\tau = \sqrt{\tau_{\text{w}}/\rho}$, where τ_{w} is the time-averaged mean shear stress at the wall. We denote the velocity normalized by the friction velocity with a superscript $^+$; i.e., $u^+ = u/u_\tau$. We also use superscript $^+$ to denote the length normalized by the inner unit length scale as $\delta_\nu := \nu/u_\tau$ and the time normalized by δ_ν/u_τ; i.e., $y^+ = y/\delta_\nu$ and $t^+ = tu_\tau/\delta_\nu$. The flow can be characterized by the friction Reynolds number defined as $Re_\tau := \delta_{99}u_\tau/\nu$, where δ_{99} is the boundary layer thickness.

We then derive the spatial state-transition matrix to obtain the solution to spatial input-output by assuming solutions of the form:

$$\psi(x, y, z, t) = \check{\psi}(x, y; \omega, \eta, k_z)e^{i(k_z z - \omega t)}e^{\eta t}, \tag{2}$$

where $k_z = 2\pi/\lambda_z$ is spanwise wavenumber and $i = \sqrt{-1}$ is the imaginary unit. η and ω respectively denote temporal growth rate and frequency, where η is introduced here for partitioning the upstream and downstream modes following Towne and Colonius [25] based on Briggs [29]'s criteria. These assumptions allow us to rewrite equation (1) as:

$$\frac{\partial}{\partial x}\check{\boldsymbol{q}}_S = \check{\boldsymbol{A}}_S\check{\boldsymbol{q}}_S + \check{\boldsymbol{B}}_{S,x}\check{f}_x, \tag{3}$$

3

where $\check{\boldsymbol{q}}_S := \begin{bmatrix} \check{u} & \check{v} & \check{v}_x & \check{w} & \check{w}_x & \check{p} \end{bmatrix}^{\mathrm{T}}$. The operators $\check{\boldsymbol{A}}_S$ and $\check{\boldsymbol{B}}_{S,x}$ are defined as:

$$
\check{\boldsymbol{A}}_S(y;\omega,\eta,k_z) := \begin{bmatrix} 0 & -\partial_y & 0 & -\mathrm{i}k_z & 0 & 0 \\ 0 & 0 & 1 & 0 & 0 & 0 \\ 0 & -Re_\tau M & Re_\tau \bar{u} & 0 & 0 & Re_\tau \partial_y \\ 0 & 0 & 0 & 0 & 1 & 0 \\ 0 & 0 & 0 & -Re_\tau M & Re_\tau \bar{u} & \mathrm{i}k_z Re_\tau \\ M & -\frac{d\bar{u}}{dy} + \bar{u}\partial_y & -\frac{\partial_y}{Re_\tau} & \mathrm{i}k_z \bar{u} & -\frac{\mathrm{i}k_z}{Re_\tau} & 0 \end{bmatrix}, \; \check{\boldsymbol{B}}_{S,x} := \begin{bmatrix} 0 \\ 0 \\ 0 \\ 0 \\ 0 \\ 1 \end{bmatrix} \tag{4}
$$

with

$$
M := \frac{1}{Re_\tau}(\partial_y^2 - k_z^2) - \eta + \mathrm{i}\omega. \tag{5}
$$

The operator similar to $\check{\boldsymbol{A}}_S$ in equation (4) is previously defined in Schmid and Henningson [30, equation (7.110)-(7.111)]. We impose boundary conditions:

$$
\check{u}(y=0) = \check{u}(y=\infty) = 0, \tag{6a}
$$
$$
\check{v}(y=0) = \check{v}(y=\infty) = 0, \quad \text{and} \tag{6b}
$$
$$
\check{w}(y=0) = \check{w}(y=\infty) = 0, \tag{6c}
$$

which correspond to no-slip at the wall and no fluctuation at the free-stream location.

In order to obtain the solution to equation (3), we need to identify the upstream and downstream modes contained in $\check{\boldsymbol{A}}_S(y;\omega,\eta=0,k_z)$ because the upstream decaying modes are growing in the downstream direction resulting in a numerical instability for downstream flow response. Here, we implement the one-way spatial equation [25] to explicitly identify upstream modes based on Briggs [29]'s criteria. Following Towne and Colonius [25], we identify the eigenvalue of $\mathrm{i}k_x(\omega,\eta=0,k_z)$ of $\check{\boldsymbol{A}}_S(y;\omega,\eta=0,k_z)$ by tracking the eigenvalues $\mathrm{i}k_x(\omega,\eta,k_z)$ of $\check{\boldsymbol{A}}_S(y;\omega,\eta,k_z)$ as a function of η. This mode $k_x(\omega,\eta=0,k_z)$ is propagating downstream if

$$
\lim_{\eta\to+\infty} \mathbb{Im}[k_x(\omega,\eta,k_z)] = +\infty, \tag{7}
$$

and propagating upstream if

$$
\lim_{\eta\to+\infty} \mathbb{Im}[k_x(\omega,\eta,k_z)] = -\infty, \tag{8}
$$

where $\mathbb{Im}[\cdot]$ represents the imaginary part of the argument. Then, we can perform an eigenvalue decomposition

$$
\check{\boldsymbol{A}}_S(y;\omega,\eta=0,k_z) = \boldsymbol{V}\boldsymbol{\Lambda}\boldsymbol{V}^{-1}, \tag{9}
$$

where $\boldsymbol{\Lambda}$ is a diagonal matrix containing eigenvalues and $\boldsymbol{V}$ is a matrix containing eigenvectors of $\check{\boldsymbol{A}}_S(y;\omega,\eta=0,k_z)$. Then, we define a matrix $\boldsymbol{D}$ that is dependent on x

$$
\boldsymbol{D}_{ii}(x) = \begin{cases} e^{\boldsymbol{\Lambda}_{ii} x}, & \text{if } \boldsymbol{\Lambda}_{ii} \text{ is downstream,} \\ 0, & \text{if } \boldsymbol{\Lambda}_{ii} \text{ is upstream.} \end{cases} \tag{10}
$$

Here, the subscript ii represents the ith diagonal element of matrix $\boldsymbol{D}$ or $\boldsymbol{\Lambda}$. The element $\boldsymbol{D}_{ii}$ is the exponential of $\boldsymbol{\Lambda}_{ii}$ multiplied by a streamwise distance x corresponding to downstream modes or is set as zero corresponding to upstream modes.

The spatial state-transition matrix mapping the state $\boldsymbol{q}_S(x_0,y;\omega,k_z)$ at $x=x_0$ to the state at another downstream location $\boldsymbol{q}_S(x_m,y;\omega,k_z)$ at $x=x_m$ at the same spatio-temporal wavenumber-frequency pair (ω,k_z); i.e., $\boldsymbol{q}_S(x_m,y;\omega,k_z) = \check{\boldsymbol{\Psi}}(x_m,x_0,y;\omega,k_z)\boldsymbol{q}_S(x_0,y;\omega,k_z)$ is given by:

$$
\check{\boldsymbol{\Psi}}(x_m,x_0,y;\omega,k_z) := \boldsymbol{V}\boldsymbol{D}(x_m-x_0)\boldsymbol{V}^{-1}. \tag{11}
$$

This spatial state-transition matrix $\check{\boldsymbol{\Psi}}$ will be employed later to compute the response due to external forcing f_x.
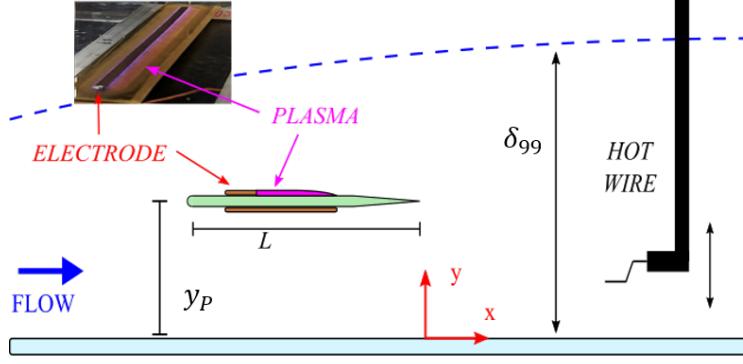
4

Fig. 2   Schematic of the experimental set-up of active large-scale structures actuator based on dielectric barrier discharge plasma.

A. Numerical method

We compute the spatial state-transition matrix in (11) by first discretizing the operators in equation (4) using the Chebyshev differential matrices generated by the MATLAB routines of Weideman and Reddy [31]. The mean profile $\bar{u}$ employed in this work is the asymptotic consistent turbulent boundary layer profile obtained from Monkewitz et al. [32]. The numerical implementation of the spatial framework is validated against the results of the spatial eigenvalue problem in Schmid and Henningson [30, figure 7.18]. We implement algebraic stretching following Schmid and Henningson [30, equations (A.53)-(A.54)], and this stretched grid is validated against eigenvalue results for Blasius boundary layer in Schmid and Henningson [30, Table A.4]. We use $N_y = 82$ grid points in the range $y^+ \in [0, 1690]$ with half of the grid points in the range of $y^+ \in [0, 345]$. The number of total grid points is increased to $N_y = 122$, and it is validated that results do not alter. We identify upstream and downstream modes in equations (7)-(8) through the `eigenshuffle` [33] function, which tracks the variation of each eigenvalue numerically based on its continuity with varying parameter η. For results in this work, we use 60 logarithmically spaced values in the range $\eta^+ \in [10^{-3}, 10]$ to approximate $\eta \to \infty$ in equations (7)-(8). We verified that this is sufficient by checking that the results do not change if we increase this to 90 logarithmically spaced values in the range $\eta^+ \in [10^{-4}, 10^2]$.

III. Comparison with experimental results

In this section, we compare the large-scale structures from the model with experimental measurements. We describe the experimental setup in subsection III.A that excites large-scale structures by plasma actuator and isolates these structures using a phase-locked analysis. Then we describe the model calibration in subsection III.B based on this experimental setup and show comparison results.

A. Experimental setup and phase-locked decomposition

Experiments were performed in one of the low-turbulence, subsonic, in-draft wind tunnels located at the Hessert Laboratory for Aerospace Research at the University of Notre Dame. The wind tunnel has an inlet contraction ratio of 6:1 and a series of 12 turbulence-management screens at the front of the inlet give rise to tunnel free stream turbulence levels of less than 0.1% (0.06% for frequencies above 10 Hz). Experiments are performed in a test section of 0.610 m square cross-section and 1.82 m in length. The experimental set-up is shown schematically in Figure 2. For this study, a two-meter long boundary layer development plate with a distributed roughness element attached to the leading edge was installed in the central height of the tunnel test section. A constant temperature anemometer (CTA) with a single boundary layer hot-wire probe (Dantec 55P15) with diameter 5 μm and length $l = 1.25$ mm was used to collect time-series of the streamwise velocity component. A computer-controlled traversing stage was inserted through the top wall of the tunnel along the midpoint of the tunnel span to allow the hot-wire probe to traverse the test section and make measurements at different wall-normal (y) locations. A plasma actuator device, as described below, was attached to the top side of the boundary layer development plate at a fixed streamwise location of 140 cm from the leading edge of the boundary layer development plate. The streamwise position of the hot-wire probe traverse system is adjustable so the probe was positioned at four streamwise (x) locations as measured downstream of the plasma actuator's trailing edge to measure the evolution of the TBL response. The streamwise locations selected for this study were 51 mm, 102 mm,

δ_{99}	U_∞	u_τ	C_f	H	Re_θ	Re_τ
34.8 mm	6.99 m/s	0.298 m/s	0.0036	1.33	1857	690

Table 1   Turbulent boundary layer parameters at the downstream location $x = 5\delta_{99}$.

170 mm, and 272 mm, which correspond to $1.5\delta_{99}$, $3\delta_{99}$, $5\delta_{99}$, and $8\delta_{99}$, respectively, based on the experimentally measured boundary layer thickness, δ_{99}, near the actuator trailing edge. A set of representative turbulent boundary layer characteristics were measured at the downstream location of $x = 5\delta_{99}$ using the hot-wire probe. These parameters are summarized in Table 1 for reference. The skin friction velocity of u_τ was found using the Clauser method. In all of the experiments described in this study, the wind tunnel free stream velocity was 7 m/s and was measured to be within $\pm 1\%$ of the expected free stream velocity before each test.

As shown in Figure 2, a plasma-based active large-scale structure actuator (ALSSA) device was used in this study to modify the dynamics of the outer layer of the boundary layer with periodic plasma-induced force. The plasma actuator was supported above the boundary layer development plate by vertical, symmetrical NACA0010 airfoils on both sides which were 4 mm thick, had a 50 mm wide chord, and was made at height intervals, y_p, from $10 - 21$ mm ($0.3\delta_{99} - 0.6\delta_{99}$). In this manner, the synthetic large-scale structures could be introduced into the TBL at different heights. The plasma actuator was $W = 25$ cm ($\approx 8\ \delta_{99}$) wide in the spanwise direction and $L = 32$ mm ($\approx 1\ \delta_{99}$) long in the streamwise direction. The actuator plate was made of a 2 mm thick sheet of Ultem dielectric polymer. An upper surface electrode of 0.05 mm thick copper foil tape was located 15 mm from the plate leading edge and was 4 mm in length and 22 cm in width. On the lower surface, a second copper foil electrode was located 15 mm from the leading edge in line with the top electrode and was 12 mm in length and 22 cm in width. The corners of the electrodes were rounded, and they were mounted in alignment to reduce extraneous regions of plasma generation and regions of highly concentrated plasma. The leading edge of the actuator plate was rounded, and the last 10 mm of the trailing edge were linearly tapered to reduce the separation region behind the trailing edge of the plate. The alternating current dielectric barrier discharge (AC-DBD) plasma formed on the actuator was produced using a high voltage AC source which consisted of a function generator, power amplifiers, and a transformer [34]. The electrodes placed on the top and bottom of the actuator were connected to the high voltage AC source which provided a 40 kV peak-to-peak sinusoidal waveform excitation to the electrodes at a frequency of 4 kHz. The peak-to-peak voltage was maintained within -5% of the expected excitation voltage during experiments. As shown in figure 2, plasma formed on the top surface of the plate above the exposed portion of the bottom surface electrode. At the 4 kHz carrier frequency, the plasma actuator operates in a quasi-steady mode, essentially creating a spanwise-uniform steady jet in the streamwise direction. To introduce periodic forcing, the sinusoidal waveform was modulated by a square wave with a fifty percent duty cycle.

The measured velocity time series were then processed by a narrow bandstop filter around 4 kHz to eliminate electronic noise associated with the high voltage AC source supplying the actuator. Since the actuator introduced periodic forcing into the flow, it is convenient to phase-locked the results to the actuation frequency. To do so, a triple phase-locked Reynolds decomposition of the velocity was considered, as shown in equation (12a) where u is the instantaneous velocity, $\bar{u}$ is the time mean component of velocity, $\tilde{u}$ is a phase-locked modal velocity component, u' is a residual fluctuating turbulent component, ϕ is the phase, defined by the relationship in equation (12b), and n is the number of realizations as described below

$$u(y,t) = \bar{u}(y) + \tilde{u}(y, \phi) + u'(y, \phi, n), \tag{12a}$$

$$\phi = \left(\frac{t_n}{T_p} - n \right) 2\pi. \tag{12b}$$

Here, t_n is a time in the nth realization, which is related to the phase angle, ϕ, by the period of the forcing repetition cycle, $T_p = 1/f_p$. The output of the function generator was used to ensure the data was phase-locked with the repetition cycle of the plasma. These n realizations are then ensemble-averaged to find the modal component of velocity, $\tilde{u}(y, \phi)$, as a function of the phase angle.

B. Model calibration and comparison results

In this subsection, we will describe the forcing model and calibrate the parameters in the spatial input-output analysis based on the experimental setup in subsection III.A and show comparison results to demonstrate the efficacy of the spatial input-output analysis described in section II in reproducing the phase-locked velocity in experiments.

Based on the actuator geometry described in III.A, We model the effect of actuation on the flow by assuming the streamwise body force $\check{f}_x$ is in the form of a Gaussian function over the wall-normal direction, a Dirac delta function over the streamwise direction, and uniform in the spanwise direction:

$$\check{f}_x(x, y; \omega, k_z) = F_0 e^{-\frac{(y-y_f)^2}{2\sigma_P^2}} \delta(x - x_0) e^{i\phi_0}, \qquad (13)$$

where F_0 represents the magnitude of this body force and ϕ_0 represents the initial phase of this body force induced by the plasma actuator. We calibrate the initial phase of the body force model as $\phi_0 = 1.15\pi$ and the magnitude as $F_0^+ = 38.2$ based on experimental measurements of phase-locked velocity at $x_m = 1.5\delta_{99}$. The values of the parameters ϕ_0 and F_0^+ do not influence the shape of phase-locked velocity due to linearity. In analog to the vibrating ribbon problem [35] in studying transitional boundary layer or signaling problem [36, 37, Section 3], the streamwise variation of this body force is modeled as a Dirac delta $\delta(x - x_0)$ function over the streamwise direction that is localized in the streamwise position x_0, which is set as $x_0 = 0$. The Gaussian function in the wall-normal direction is motivated by [38, 39], where this function is also employed to model localized forcing. y_f and σ_p in the Gaussian function are respectively the center of the peak and standard deviation determining the wall-normal shape of plasma-induced body force. We set $\sigma_p^+ = 60$ and the body force center to be $y_f = 0.13\delta_{99} + y_p$, i.e., $0.13\delta_{99}$ higher than the actuator plate height. This height correction and the standard deviation σ_p^+ in forcing function are employed to match the peak of phase-locked velocity in experiments at $x_m/\delta_{99} = 1.5$ induced by the ALSSA devise actuation. The calibrated values F_0^+, ϕ_0, y_f, and σ_p^+ are kept the same in this work. The spanwise wavenumber in equation (4) is chosen as $k_z = 0$ as the plasma actuation in the experiment is spanwise uniform and the fact that the experimental measurements of flow response do not show significant spanwise variation. Here, we set the frequency to $\omega^+ = 2\pi f_p^+$ to match that of the plasma actuation. We specify the Reynolds number $Re_\tau = 690$ to match experimental measurements in both the determination of the mean velocity profile and the computations.

The corresponding solution of equation (3) at downstream measurement position x_m with respect to the streamwise localized forcing $\check{f}_x$ can be computed using the spatial state-transition matrix in (11):

$$\check{q}_S(x_m, y; \omega, k_z) = \check{\mathbf{\Psi}}(x_m, x_0, y; \omega, k_z) \check{\mathbf{B}}_{S,x} F_0 e^{-\frac{(y-y_f)^2}{2\sigma_P^2}} e^{i\phi_0}. \qquad (14)$$

In order to compare with hot-wire measurements described in III.A, we obtain streamwise velocity as:

$$\check{u} = \check{\mathbf{C}}_{S,u}\check{q}_S, \quad \check{\mathbf{C}}_{S,u} := \begin{bmatrix} 1 & 0 & 0 & 0 & 0 & 0 \end{bmatrix}. \qquad (15a,b)$$

Based on the computation of phase-locked velocity from experiments in equation (12), we can similarly obtain the phase-locked velocity at a certain downstream measurement location x_m by multiplying $e^{-i\phi}$ to shift the phase:

$$\tilde{u}(x_m, y; \omega, k_z, \phi) = \mathbb{Re}[\check{u}(x_m, y; \omega, k_z)e^{-i\phi}], \qquad (16)$$

where $\mathbb{Re}[\cdot]$ represents the real part of the argument.

We compare the phase-locked velocity obtained from the proposed spatial input–output analysis against results from experimental measurements associated with an actuation frequency $f_p = 80$ Hz ($0.3983U_\infty/\delta_{99}$ and $f_p^+ = 0.0135$) and the actuator plate height $y_p/\delta_{99} = 0.3$. This actuator plate height $y_p/\delta_{99} = 0.3$ corresponds to the top boundary of the log-law layer [40]. Figure 3 compares the phase-locked velocity at four different downstream measurement locations $x_m/\delta_{99} = 1.5$, $x_m/\delta_{99} = 3$, $x_m/\delta_{99} = 5$, and $x_m/\delta_{99} = 8$ from experimental measurements (top panels) and the model (bottom panels). In all panels, the long black dashed line (– –, black) corresponds to the height of actuator plate y_p and the short black solid line (—, black) is the height of the body force center y_f modeling the effect of plasma actuation. Here, we can see that the model provides reasonable agreement with experimental measurement. Both the experimental results and the model show that the phase-locked velocity $\tilde{u}$ at the central regions are decaying as they propagate downstream. This downstream spatio-temporal characteristic of the phase lock velocity as it decays was recently highlighted using particle image velocimetry (PIV) measurements that directly track the streamwise evolution of the velocity field [21]. The experimental results show that the velocity at the bottom region at (b) $x_m/\delta_{99} = 3$ is larger than that at (a) $x_m/\delta_{99} = 1.5$, a trend that is also reflected in the model prediction in panels (e) and (f).

IV. Downstream propagation of large-scale structures

Aside from the streamwise velocity, the wall-normal velocity is also typically measured by PIV; e.g., [12, 21]. Using the combined information of streamwise and wall-normal velocity can also provide insight into the influence of
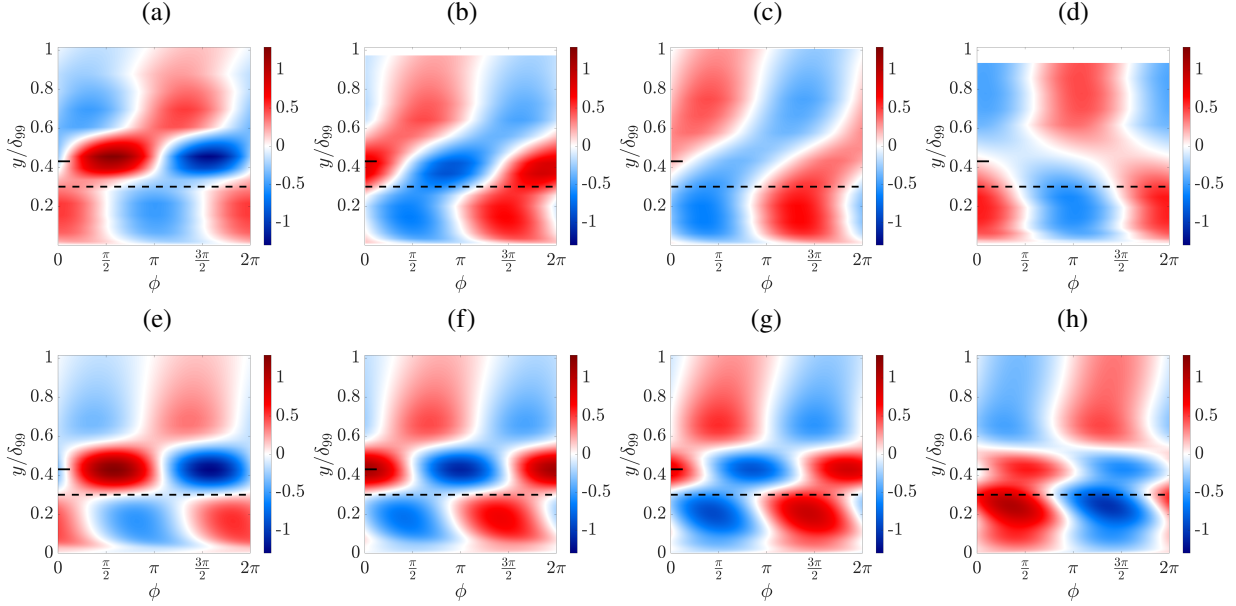
Fig. 3 **A comparison of phase-locked modal velocity $\tilde{u}^+$ measured from experiments in** (12) **against the results from model $\tilde{u}^+$ in** (16) **with the plasma actuator height $y_p/\delta_{99} = 0.3$, actuation frequency $f_p = 80$ Hz. The top four panels are results from experimental measurements $\tilde{u}^+$ with the downstream measurement location (a) $x_m/\delta_{99} = 1.5$, (b) $x_m/\delta_{99} = 3$, (c) $x_m/\delta_{99} = 5$, and (d) $x_m/\delta_{99} = 8$. The bottom four panels are results from spatial input-output analysis $\tilde{u}^+$ with the downstream measurement location (e) $x_m/\delta_{99} = 1.5$, (f) $x_m/\delta_{99} = 3$, (g) $x_m/\delta_{99} = 5$, and (h) $x_m/\delta_{99} = 8$. In all panels, (– –) represents plate height $y_p/\delta_{99} = 0.3$ employed in experiments; and (—) represents the body force center $y_f = y_p + 0.13\delta_{99}$ employed in the body force model in equation** (13).

large-scale structures on Reynolds shear stress. As a result, we also modify the output operator to obtain the wall-normal velocity:

$$\check{v} = \check{\boldsymbol{C}}_{S,v}\check{\boldsymbol{q}}_S, \quad \check{\boldsymbol{C}}_{S,v} := \begin{bmatrix} 0 & 1 & 0 & 0 & 0 & 0 \end{bmatrix}. \tag{17}$$

Because the flow is mainly characterized by (u, v) velocity in the (x, y) plane and nearly uniform in the spanwise direction, the vorticity of interest is spanwise vorticity that can be also obtained by modifying output operator:

$$\check{\omega}_z = \check{\boldsymbol{C}}_{S,\omega_z}\check{\boldsymbol{q}}_S, \quad \check{\boldsymbol{C}}_{S,\omega_z} := \begin{bmatrix} -\partial_y & \partial_x & 0 & 0 & 0 & 0 \end{bmatrix}. \tag{18}$$

The downstream evolution of large-scale structures is also of interest in canonical wall-bounded turbulent flows [41]. Aside from performing a phase-locked analysis by modifying the phase, this spatial input-output analysis can also provide the downstream evolution of phase-locked velocity by directly changing different downstream measurement locations x_m. We define:

$$u_s(x_m, y; \omega, k_z) = \mathbb{Re}[\check{u}(x_m, y; \omega, k_z)], \tag{19a}$$

$$v_s(x_m, y; \omega, k_z) = \mathbb{Re}[\check{v}(x_m, y; \omega, k_z)], \tag{19b}$$

$$\omega_{z,s}(x_m, y; \omega, k_z) = \mathbb{Re}[\check{\omega}_z(x_m, y; \omega, k_z)]. \tag{19c}$$

Figure 4(a) presents the u_s^+ as a function of streamwise measurement location x_m and wall-normal height y. The spatial evolution shown in figure 4 is not perfectly periodic in the spatial domain, which is due to different convective velocities at different heights embedded within the turbulent mean velocity profile. This is the benefit of the spatial input-output analysis that does not require selecting a specific streamwise wavenumber but directly performing downstream marching. Here, we can see that near the inflow region, u_s^+ in panel (a) shows alternating positive and negative values over the wall-normal direction, with phase jumps evident at the two wall-normal locations separating the top, central, and bottom regions. Moving downstream, one can see that the flow at the central region is traveling

8

faster than that at the bottom region. The dotted line ($\cdots$) in figure 4 (a) measures the downstream distance after three periods, which shows the effect of wall-normal dependent convective velocity. A direct result of this is the shape of phase-locked velocity observed in figure 3.

The wall-normal velocity component of phase-locked velocity v_s^+ is shown in figure 4(b). Here, positive and negative values are seen at the region above or below the center of the forcing y_f near the inflow region $x_m = 0$, but farther downstream, the wall-normal velocity is more uniform across the wall-normal height. Figure 4(c) presents the spanwise vorticity $\omega_{z,s}^+$ as contour with velocity vectors (u_s, v_s) superimposed. Here, we can see that this body force model generates counter-rotating spanwise vorticity near the inflow region. As the actuated large-scale structures are propagating downstream, the bottom spanwise vorticity is more inclined towards the wall.

Next, we combine our proposed input-output framework with quadrant analysis [26, 27] to study the impact of the large-scale structures resulting from actuation on the Reynolds shear stress. The quadrants are defined in terms of u_s and v_s phase-locked velocities. We adopt the traditions definitions in which the first quadrant Q1 corresponds to outward interactions ($u_s > 0, v_s > 0$), the second quadrant Q2 is ejection ($u_s < 0, v_s > 0$), the third quadrant Q3 corresponds to inward interactions ($u_s < 0, v_s < 0$) and the fourth quadrant Q4 is sweep ($u_s > 0, v_s < 0$) [27]. Figure 4(d) plots these quadrants as a contour with velocity vectors (u_s, v_s) superimposed. Figure 4(d) shows that at the central region close to the actuator $x_m = 0$, the Q4 and Q2 quadrant events are the strongest, and they are spreading towards the top and bottom regions moving downstream. Moving from the upstream to downstream direction, we can see the quadrant events in the order Q4→Q3→Q2→Q1 at the top region, but at the bottom region, the quadrant events are in the order of Q1→Q2→Q3→Q4. This is consistent with the counter-rotating vorticity patterns appearing in the top and bottom regions as shown in figure 4(c). The quadrant trajectory analysis was previously employed to characterize 36 distinct evolution patterns for (u, v) in turbulent pipe flow and the trajectories Q2→Q1→Q4, Q2→Q3→Q4, Q4→Q1→Q2, and Q4→Q3→Q2 were shown to play the most important role in the dynamics and transport of near-wall turbulence [28]. These four important quadrant trajectories are also observed here by actuated large-scale structures as outlined in four different boxes in figure 4(d). The results in figure 4 demonstrate that the spatial input-output analysis can provide detailed downstream evolution of actuated large-scale structures.

V. Conclusions and future work

This work proposes spatial input–output analysis for analyzing the behavior of large-scale structures in actuated turbulent boundary layers. This framework employs downstream marching based on recently developed one-way spatial integration [25] in order to overcome ambiguity imposed by the need to specify streamwise wavenumber in input–output (resolvent) analysis. In particular, this downstream marching embeds a wall-normal dependent convective velocity for actuated large-scale structures associated with a dominant temporal frequency. The effect of the plasma actuator is modeled as a streamwise body force localized in streamwise and wall-normal direction resembling impulse forcing [35, 38]. The results are compared with large-scale structures in experimental measurements, where the perturbation is introduced through a dielectric barrier discharge plasma actuator, and the shape of large-scale structures is obtained through hot-wire anemometry measurements and a phase-locked analysis.

Large-scale structures obtained from this spatial input–output analysis show qualitative agreements with experimental measurements. As the actuated large-scale structures propagate downstream, they are more inclined towards the wall resulting from convective velocities that vary with distance from the wall.

Our analysis is then employed to quantify the impact on momentum transfer of such coherent motion by evaluating the ejection-sweep cycle via quadrant analysis [26, 27]. The obtained quadrant orders Q4→Q3→Q2→Q1 at the top region and Q1→Q2→Q3→Q4 at the bottom region share similarities with canonical wall-bounded turbulent flows without forcing [28], which implies that our actuation creates structures consistent with those in canonical wall-bounded turbulent flows.

The results demonstrate that the proposed spatial input-output analysis can provide insights into the large-scale flow structures induced by temporally periodic and spatially localized perturbations in wall-bounded turbulent flows.
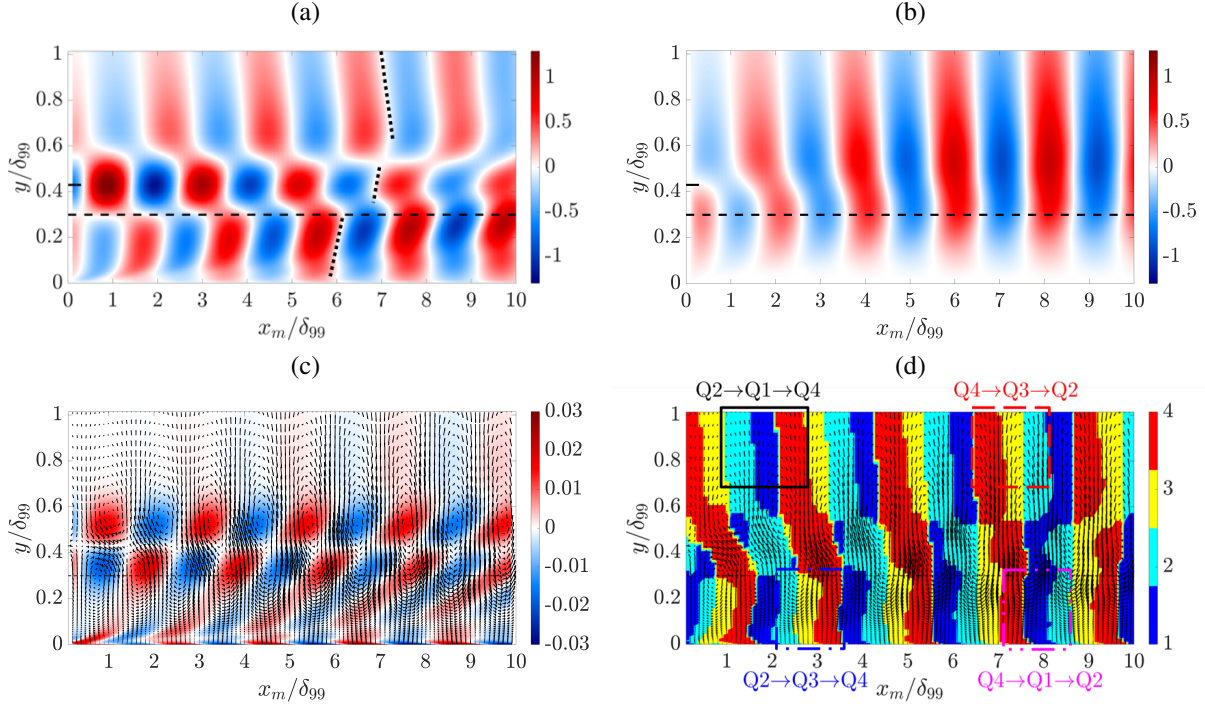
Acknowledgment

Fig. 4   Downstream evolution of (a) u_s^+, (b) v_s^+, and (c) spanwise vorticity $\omega_{z,s}^+$ with $f_p = 80$ Hz, $y_p/\delta_{99} = 0.3$. The dotted line ($\cdots$) in panel (a) measures the downstream distance after three periods. The contour in panel (d) is presenting quadrant numbers. The arrows in panels (c) and (d) are presenting (u_s^+, v_s^+). In panel (d), the box outlined by (—) represents Q2→Q1→Q4, the box outlined by (– –) represents Q4→Q3→Q2, the box outlined by (– · –) represents Q2→Q3→Q4, and the box outline by (– · · –) represents Q4→Q1→Q2. In all panels, long horizontal line (– –) represents plate height $y_p/\delta_{99} = 0.3$ employed in experiments; and short horizontal line (—) represents the body force center $y_f = y_p + 0.13\delta_{99}$ employed in the body force model in equation (13).

References

[1] Balakumar, B., and Adrian, R., "Large- and very-large-scale motions in channel and boundary-layer flows," *Philos. Trans. R. Soc. London A Math. Phys. Eng. Sci.*, Vol. 365, No. 1852, 2007, pp. 665–681.

[2] Guala, M., Hommema, S. E., and Adrian, R. J., "Large-scale and very-large-scale motions in turbulent pipe flow," *J. Fluid Mech.*, Vol. 554, 2006, pp. 521–542.

[3] Mathis, R., Hutchins, N., and Marusic, I., "Large-scale amplitude modulation of the small-scale structures in turbulent boundary layers," *J. Fluid Mech.*, Vol. 628, 2009, pp. 311–337.

[4] Mathis, R., Monty, J. P., Hutchins, N., and Marusic, I., "Comparison of large-scale amplitude modulation in turbulent boundary layers, pipes, and channel flows," *Phys. Fluids*, Vol. 21, No. 11, 2009, pp. 1–4.

[5] Marusic, I., McKeon, B. J., Monkewitz, P. A., Nagib, H. M., Smits, A. J., and Sreenivasan, K. R., "Wall-bounded turbulent flows at high Reynolds numbers: Recent advances and key issues," *Phys. Fluids*, Vol. 22, No. 6, 2010, p. 065103.

[6] Hwang, J., and Sung, H. J., "Influence of large-scale motions on the frictional drag in a turbulent boundary layer," *J. Fluid Mech.*, Vol. 829, 2017, pp. 751–779.

[7] Abbassi, M., Baars, W., Hutchins, N., and Marusic, I., "Skin-friction drag reduction in a high-Reynolds-number turbulent boundary layer via real-time control of large-scale structures," *Int. J. Heat Fluid Flow*, Vol. 67, 2017, pp. 30–41.

[8] Corke, T. C., and Thomas, F. O., "Active and passive turbulent boundary-layer drag reduction," *AIAA J.*, Vol. 56, No. 10, 2018, pp. 3835–3847.

[9] Hussain, A. K. M. F., and Reynolds, W. C., "The mechanics of an organized wave in turbulent shear flow," *J. Fluid Mech.*, Vol. 41, No. 2, 1970, pp. 241–258.

[10] Hussain, A. K. M. F., and Reynolds, W. C., "The mechanics of an organized wave in turbulent shear flow. Part 2. Experimental results," *J. Fluid Mech.*, Vol. 54, No. 2, 1972, pp. 241–261.

[11] Jacobi, I., and McKeon, B. J., "New perspectives on the impulsive roughness-perturbation of a turbulent boundary layer," *J. Fluid Mech.*, Vol. 677, 2011, pp. 179–203.

[12] Jacobi, I., and McKeon, B. J., "Dynamic roughness perturbation of a turbulent boundary layer," *J. Fluid Mech.*, Vol. 688, 2011, pp. 258–296.

[13] Jacobi, I., and McKeon, B. J., "Phase relationships between large and small scales in the turbulent boundary layer," *Exp. Fluids*, Vol. 54, No. 3, 2013, p. 1481.

[14] McKeon, B. J., Jacobi, I., and Duvvuri, S., "Dynamic roughness for manipulation and control of turbulent boundary layers: an overview," *AIAA J.*, Vol. 56, No. 6, 2018, pp. 2178–2193.

[15] Ranade, P., Duvvuri, S., McKeon, B., Gordeyev, S., Christensen, K., and Jumper, E. J., "Turbulence amplitude amplification in an externally forced, subsonic turbulent boundary layer," *AIAA J.*, Vol. 57, No. 9, 2019, pp. 3838–3850.

[16] Lozier, M., Midya, S., Thomas, F. O., and Gordeyev, S., "Experimental studies of boundary layer dynamics using active flow control of large-scale structures," *Proceedings of the Eleventh International Symposium on Turbulence and Shear Flow Phenomenon*, Southampton, UK, 2019.

[17] Lozier, M. E., Thomas, F. O., and Gordeyev, S., "Streamwise evolution of turbulent boundary layer response to active control actuator," *AIAA Scitech 2020 Forum*, 2020, p. 0097.

[18] Lozier, M. E., Thomas, F. O., and Gordeyev, S., "Turbulent Boundary Layer Response to Active Control Actuator," *AIAA Scitech 2021 Forum*, 2021, p. 1455.

[19] Reynolds, W. C., and Hussain, A. K. M. F., "The mechanics of an organized wave in turbulent shear flow. Part 3. Theoretical models and comparisons with experiments," *J. Fluid Mech.*, Vol. 54, No. 2, 1972, pp. 263–288.

[20] McKeon, B. J., and Sharma, A. S., "A critical-layer framework for turbulent pipe flow," *J. Fluid Mech.*, Vol. 658, 2010, pp. 336–382.

[21] Huynh, D., and McKeon, B., "Characterization of the spatio-temporal response of a turbulent boundary layer to dynamic roughness," *Flow Turbul. Combust.*, Vol. 104, No. 2, 2020, pp. 293–316.

[22] Taylor, G. I., "The spectrum of turbulence," *Proc. R. Soc. London A Math. Phys. Eng. Sci.*, Vol. 164, No. 919, 1938, pp. 476–490.

[23] Kreiss, H. O., "Initial boundary value problems for hyperbolic systems," *Commun. Pure Appl. Math.*, Vol. 23, No. 3, 1970, pp. 277–298.

[24] Trefethen, L. N., and Halpern, L., "Well-posedness of one-way wave equations and absorbing boundary conditions," *Math. Comput.*, Vol. 47, No. 176, 1986, pp. 421–435.

[25] Towne, A., and Colonius, T., "One-way spatial integration of hyperbolic equations," *J. Comput. Phys.*, Vol. 300, 2015, pp. 844–861.

[26] Wallace, J. M., Eckelmann, H., and Brodkey, R. S., "The wall region in turbulent shear flow," *J. Fluid Mech.*, Vol. 54, No. 1, 1972, pp. 39–48.

[27] Wallace, J. M., "Quadrant Analysis in Turbulence Research : History and Evolution," *Annu. Rev. Fluid Mech.*, Vol. 4, 2016, pp. 131–158.

[28] Nagano, Y., and Tagawa, M., "Coherent motions and heat transfer in a wall turbulent shear flow," *J. Fluid Mech.*, Vol. 305, 1995, pp. 127–157.

[29] Briggs, R. J., *Electron-stream interaction with plasmas*, MIT, 1964.

[30] Schmid, P. J., and Henningson, D. S., *Stability and transition in shear flows*, Vol. 142, Springer Science & Business Media, 2012.

[31] Weideman, J. A. C., and Reddy, S. C., "A MATLAB differentiation matrix suite," *ACM Trans. Math. Softw.*, Vol. 26, No. 4, 2000, pp. 465–519.

[32] Monkewitz, P. A., Chauhan, K. A., and Nagib, H. M., "Self-consistent high-Reynolds-number asymptotics for zero-pressure-gradient turbulent boundary layers," *Phys. Fluids*, Vol. 19, No. 11, 2007, p. 115101.

[33] D'Errico, J., "Eigenshuffle (https://www.mathworks.com/matlabcentral/fileexchange/22885-eigenshuffle)," *MATLAB Central File Exchange.*, 2020.

[34] Thomas, F. O., Corke, T. C., Iqbal, M., Kozlov, A., and Schatzman, D., "Optimization of dielectric barrier discharge plasma actuators for active aerodynamic flow control," *AIAA J.*, Vol. 47, No. 9, 2009, pp. 2169–2178.

[35] Ashpis, D. E., and Reshotko, E., "The vibrating ribbon problem revisited," *J. Fluid Mech.*, Vol. 213, 1990, pp. 531–547.

[36] Huerre, P., Batchelor, G. K., Moffatt, H. K., and Worster, M. G., "Open shear flow instabilities," *Perspectives in fluid dynamics*, 2000, pp. 159–229.

[37] Huerre, P., and Monkewitz, P. A., "Absolute and convective instabilities in free shear layers," *J. Fluid Mech.*, Vol. 159, 1985, pp. 151–168.

[38] Jovanovic, M., and Bamieh, B., "The spatio-temporal impulse response of the linearized Navier-Stokes equations," *Proceedings of the 2001 American Control Conference.(Cat. No. 01CH37148)*, Vol. 3, IEEE, 2001, pp. 1948–1953.

[39] Vadarevu, S. B., Symon, S., Illingworth, S. J., and Marusic, I., "Coherent structures in the linearized impulse response of turbulent channel flow," *J. Fluid Mech.*, Vol. 863, 2019, pp. 1190–1203.

[40] Pope, S. B., *Turbulent flows*, Cambridge university press, Cambridge, England, 2000.

[41] Adrian, R. J., "Hairpin vortex organization in wall turbulence," *Phys. Fluids*, Vol. 19, No. 4, 2007, p. 041301.